International Journal of Solids and Structures 51 (2014) 2990–3001

Contents lists available at ScienceDirect

International Journal of Solids and Structures

journal homepage: www.elsevier.com/locate/ijsolstr

Dynamic response of a growing inclusion in a discrete system

M.J. Nieves [a,*], I.S. Jones [a], A.B. Movchan [b]

[a] School of Engineering, Liverpool John Moores University, James Parsons Building, Byrom Street, Liverpool L3 3AF, UK
[b] Department of Mathematical Sciences, University of Liverpool, Peach Street, Liverpool L69 3BX, UK

ARTICLE INFO

Article history:
Received 7 August 2013
Received in revised form 13 March 2014
Available online 20 April 2014

Keywords:
Semi-infinite line defects
Infinite square-cell lattice
Wiener–Hopf technique
Dispersion
Localisation

ABSTRACT

The propagation of a semi-infinite line defect, contained in an infinite square-cell lattice is considered. The defect is composed of particles lighter than those in the ambient lattice and it is assumed this defect propagates with constant speed. Dispersion properties of the lattice are related to waves generated by the propagating defect. In order to determine these properties, the Wiener–Hopf technique is applied. Additional features, related to localisation along the defect are also identified. Analysis of the dispersion relations for this lattice, from the kernel function inside the Wiener–Hopf equation, is carried out. The solution of the Wiener–Hopf equation is presented for the case when an external load is applied corresponding to an energy flux at infinity.

1. Introduction

Large deformations occurring in composite materials can lead to regions of plastic flow, where the formation of line inclusions can occur (Özturk et al., 1991). When waves propagate through a composite, defects within the composite can lead to localised defect modes i.e. large deformations around the defects (Movchan et al., 2007). Such large deformations can also drive the growth of a defect or an inclusion through a composite. In this article, the model for a growing line inclusion within a discrete lattice, having particles which are lighter than those in the ambient lattice, is considered. The model provides information of dispersion properties of the lattice, and at particular frequencies, waves travelling through the lattice may propagate only along the inclusion or the ambient lattice. The former situation may enhance the growth of the inclusion through the lattice and therefore it is important to determine the frequencies which generate such vibrating modes.

Lattice models describing defects propagating through discrete structures have been the subject of many articles. In Slepyan (2001a), the scalar problem of a dynamic crack moving with constant speed through a homogeneous square-cell lattice is studied. The dynamic crack can be considered as a sequential removal of neighbouring bonds, along a row in the lattice, caused by feeding waves which supply energy to the crack front bond (Slepyan, 2002). When this bond breaks, energy is released in the form of dissipative waves which carry energy away from the front. The problem of a fault moving through an elastic triangular lattice was studied in Slepyan (2001c). For both the square and triangular lattices, the wave dispersion properties for the lattice can be deduced in explicit form.

Apart from the introduction of the dynamic crack, additional inhomogeneities which also affect the dispersion properties in a lattice or a continuum can be considered. An overview of several models that reveal the dispersive nature of waves in continua and periodic structures was presented in Movchan et al. (2012), which also includes comparisons of the filtering effects of a bi-atomic chain and a high-contrast periodic continuum. The problem of a structured interface contained in a continuum was also solved and the reflection and transmission due to the interface were analysed. In Mishuris et al. (2009a), a square-cell lattice containing a propagating crack, and composed of rows of particles having contrasting mass, was analysed. The influence of this additional inhomogeneity on the energy dissipation due to crack propagation was also considered.

An inhomogeneous triangular lattice, composed of bonds with contrasting stiffness in the principal lattice directions, can be found in Nieves et al. (2013). This is based on a similar model of that developed in Slepyan (2001c).

In all the above linear models, interaction between the particles of the lattice is assumed to occur between the nearest neighbours and the bonds connecting particles are assumed to be massless. From these models, other useful properties of the fault, such as the energy release rate may also be obtained.

In some of these models (Colquitt et al., 2012; Mishuris et al., 2009b), a fracture criterion has been used to obtain information about real time progression of the crack. In particular, this can

* Corresponding author. Tel.: +44 151 231 2011.
E-mail address: M.J.Nieves@ljmu.ac.uk (M.J. Nieves).

http://dx.doi.org/10.1016/j.ijsolstr.2014.03.034
0020-7683/

reveal information about the formation and coalescence of voids ahead of the crack front bond. An inhomogeneous square-cell lattice containing a propagating fault, subjected to a remote sinusoidal load was considered in Mishuris et al. (2009b). When a fracture criterion is imposed on the crack path bonds, the problem becomes non-linear. Numerical simulations have been used to calculate average crack speeds and a good comparison has been found with estimates from dispersion diagrams. Similar calculations for an inhomogeneous triangular lattice have been carried out in Colquitt et al. (2012). Extensions of this analysis have been used to predict the propagation of an edge crack in a structured thermo-elastic solid, where the crack propagation is driven by rapid change in boundary temperature near the interface the crack emanates from and the elastic waves generated by shocks induced by the rapid temperature change (Carta et al., 2013).

It is also possible to find continuum models where the influence of the material's microstructure may be studied. The theory of couple-stress elasticity introduced in Koiter (1964), is designed to take into account characteristic lengths associated with bending and torsion within a material, and this allows the microstructural properties of a material to be studied. In Mishuris et al. (2012), this model was used to study a Mode III semi-infinite crack propagating at constant speed through a continuum that has a microstructure. The Wiener–Hopf technique was also applied to solve this problem and illustrations showing the effect of the material's bending and torsion characteristic lengths on the crack's propagation were presented. The method was also extended to the case of a Mode III crack propagating through an elastic material having a high rotational inertia introduced through its microstructure in Morini et al. (2013). There, the influence of the micro-rotational inertia on the energy dissipation due to crack propagation was also analysed, as this dissipation can affect displacements in the vicinity of the crack tip. It was shown that this rotational inertia may enhance or diminish the energy dissipation associated with the propagating crack, in comparison to its energy dissipation in the model of classical elasticity.

The influence of the microstructure can also be determined from models of discrete structures which have the same effective properties as the corresponding homogenised medium. As an example, the effect of the microstructure on the crack-tip behaviour for an edge crack contained in a slab, which is subjected to a sinusoidal temperature load, was also investigated in Colquitt et al. (2012). For this quasi-static thermoelastic problem, it was shown that the "effective stress intensity factor" for the edge crack in the triangular lattice was lower than that in the homogenised lattice. This indicates that the introduction of microstructure in a solid may lessen the possibility of crack propagation.

For the high-frequency regime of the applied load, a theory of asymptotic homogenisation has been developed in Craster et al. (2010). A continuum model is constructed from the standing wave modes for the lattice problem, and the solution of this continuum problem provides information about the microstructure.

The propagation of an inclusion within a lattice has also been considered in Slepyan (2001b). Here, instead of the removal of subsequent bonds in a row, giving rise to a crack, these bonds undergo a transition in phase, i.e. a jump in stiffness, when the elongation of the bonds reaches a critical point. Another way to interpret the propagation of an inclusion within the lattice is to assume that the inclusion is composed of particles of different mass to those in the ambient lattice. This is discussed in the present paper. The required dispersion properties are obtained from Colquitt et al. (2013), where eigenfrequencies and eigenmodes, corresponding to localised defect modes, for a finite line defect contained in a square lattice were computed. For a long line defect, these eigenfrequencies have been shown to lie in the range of frequencies predicted by the model for the infinite line defect (Osharovich and Ayzenberg-Stepanenko, 2012). An illustrative example given in Colquitt et al. (2013), shows a computation for the eigenfrequencies for a line defect containing 20 particles having contrasting mass compared to the ambient lattice. On Fig. 1, these frequencies are shown by dashed horizontal lines. The solid curve in this figure, depicts the dispersion curve of the infinite line defect model of Osharovich and Ayzenberg-Stepanenko (2012), and it is possible to see from this figure that this model can be used to predict the complete range of the frequencies for a long finite line defect. The same dispersion relation is also encountered in the work presented here. It is also noted that the density of the eigenfrequencies for the finite line defect shown in Fig. 1, increases as we approach the frequencies of the standing wave modes for the infinite line defect, where the homogenised model for this defect is applicable.

The diffraction of waves due to a semi-infinite line of rigid small inclusions within a continuum, called a grating, has been studied in Hills and Karp (1965). This problem has been solved using the Wiener–Hopf technique (Noble, 1958; Hochstadt, 1989) and this solution has used to describe resonance modes for the grating as well as the dispersive nature of this line defect (Hills, 1965; Hills and Karp, 1965).

For finite length rigid line inclusions contained in an elastic material, the complete solution has been obtained for this problem in the case of when the ambient matrix is a bimaterial and the rigid line inclusion is located along the interface of the two materials Ballarini, 1990. Here the strength of the singularities found in the solution near the tips of the inclusion have been determined and compared with those in the problem of when there is a crack along the interface in the bimaterial. A similar analysis has been given in Dal Corso et al. (2008) and Bigoni et al. (2008), where the model for a prestressed elastic material containing a rigid line inclusion under Mode I and II loading has been considered. The influence of the inclusion on the fracture patterns in this problem was also studied and the analytical results were shown to give a good agreement with those obtained in experiments.

A semi-infinite line defect is considered here which propagates through a square-cell lattice. The structure of this article is as follows. In Section 2, the problem of the propagating semi-infinite fault, composed of particles with reduced mass compared to the ambient infinite square lattice, is analysed. The description of this problem and the main notations are given in Section 2.1. In Section 2.2, the dynamic equations are introduced for the

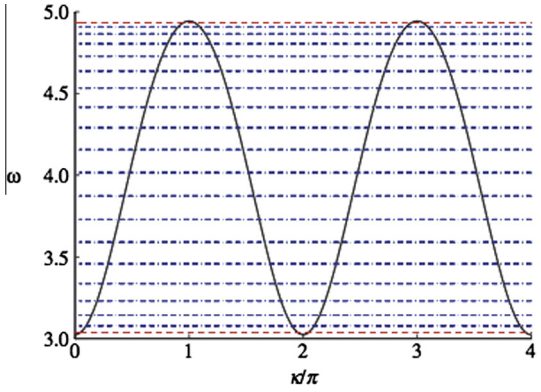

Fig. 1. Example computation from Colquitt et al. (2013), showing the comparison of the eigenfrequencies (ω) computed for a line defect composed of 20 particles with different mass compared to that of the particles in the ambient lattice (indicated by horizontal dashed lines) and the curve given for the infinite line defect in the lattice (Osharovich and Ayzenberg-Stepanenko, 2012). Both are shown as functions of the normalised wavenumber κ/π. Here the ratio of the mass of the particles in the line defect to the mass of the particles in the ambient lattice is 0.25.

propagating semi-infinite defect inside the lattice, and the procedure for solving this problem is given, including the reduction of this problem to a Wiener–Hopf equation posed on the line of the defect. From the roots and poles of the kernel function in this equation, dispersion relations for the defect moving with constant speed are then determined in Section 2.3. For a given speed of the propagating defect, a description of the roots and poles of the kernel function is outlined in Section 2.4, and this information is used to study the Wiener–Hopf equation and derive its solution in Section 3. In Section 4, for a particular load, the solution of the Wiener–Hopf equation is derived and the local displacements of the defect are compared with the asymptotics of the displacement that gives the behaviour of the solution in the vicinity of the defect in the corresponding homogenised problem. The Fourier transform of the discontinuous inertia term and a proof that the index of the kernel function is zero are given in Appendices A and B, respectively. In Appendix C, the general solution for the Wiener–Hopf equation of Section 2 is also presented.

2. Dynamic semi-infinite chain inside the lattice

2.1. Main notations and description of the problem

The problem of a semi-infinite line defect, composed of particles of mass m, propagating through a square-cell lattice, composed of particles of mass M, is now discussed. It is assumed that $m < M$. This defect is located along $n = 0,\ k \leqslant -1$ (see Fig. 2), and it is assumed that the bonds connecting the particles within the lattice have stiffness μ.

The semi-infinite line defect propagates with constant speed v through the lattice. As it does so, this represents a succession of phase transitions as the mass of the particles along $n = 0$ change value. The time interval between successive phase transitions is a/v (where a is the bond length which is normalised to 1).

The variable $\eta = x - vt$, where $x = ka$, is used to define a moving coordinate system, with centre $\eta = 0,\ n = 0$ (see Slepyan, 2002).

It is assumed that displacements within the lattice are functions of η, i.e. the displacement $u_{k,n}$ of the particle with position (k, n) within the lattice, is assumed to have the form

$$u_{k,n}(t) = u_n(\eta). \tag{2.1}$$

About the line $n = 0$, the displacements satisfy the symmetry condition

$$u_n(\eta) = u_{-n}(\eta), \quad \text{for } n \geqslant 0. \tag{2.2}$$

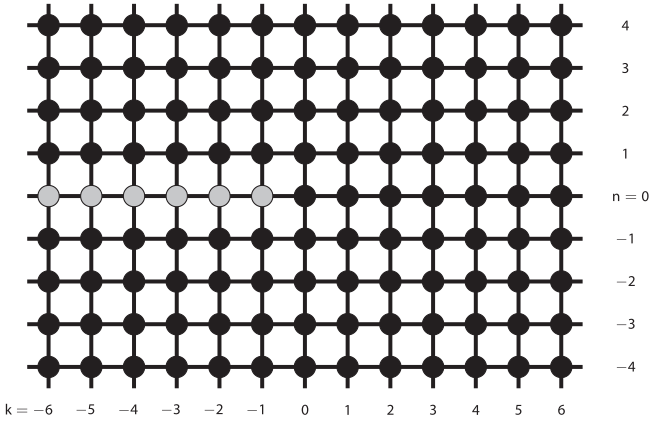

Fig. 2. A square cell lattice containing a semi-infinite chain of particles having mass m along $n = 0$, and the ambient lattice is composed of particles with mass M $(m < M)$. All links are assumed to have stiffness μ.

The function $u_n(\eta)$ can be split according to

$$u_n(\eta) = u_n^+(\eta) + u_n^-(\eta), \tag{2.3}$$

with

$$u_n^+(\eta) = H(\eta)u_n(\eta), \quad \text{and} \quad u_n^-(\eta) = (1 - H(\eta))u_n(\eta),$$

with H being the Heaviside function. The left and right-sided Fourier transforms are also used

$$u_n^{F,+}(\xi) = \int_0^\infty u_n^+(\eta)e^{i\xi\eta}\,d\eta, \quad \text{Im } \xi > 0,$$

$$u_n^{F,-}(\xi) = \int_{-\infty}^0 u_n^-(\eta)e^{i\xi\eta}\,d\eta, \quad \text{Im } \xi < 0.$$

These transforms lead to the definitions

$$u_{n,\pm}^F(\xi) = \lim_{\text{Im}\xi\to 0} u_n^{F,\pm}(\xi),$$

and then the continuous Fourier transform of the displacement u_n

$$u_n^F(\xi) = \int_{-\infty}^\infty u_n(\eta)e^{i\xi\eta}\,d\eta,$$

can be written using the additive split:

$$u_n^F = u_{n,+}^F + u_{n,-}^F. \tag{2.4}$$

2.2. The model for a propagating semi-infinite line defect in a square lattice

Here, the model describing the propagation of a semi-infinite line defect is presented. The problem will be shown to reduce to a Wiener–Hopf equation along $n = 0$.

2.2.1. Dynamic equations of motion

Due to symmetry (2.2) only the upper lattice half plane is considered. The equations of motion $(n \geqslant 1)$ have the form

$$M\frac{d^2u_{k,n}}{dt^2}(t) = \mu(u_{k+1,n}(t) + u_{k-1,n}(t) + u_{k,n+1}(t) + u_{k,n-1}(t) - 4u_{k,n}(t)) \tag{2.5}$$

and for $n = 0$, if $k < vt$,

$$m\frac{d^2u_{k,0}}{dt^2}(t) = \mu(u_{k+1,0}(t) + u_{k-1,0}(t) + u_{k,1}(t) + u_{k,-1}(t) - 4u_{k,0}(t)) + q_k(t), \tag{2.6}$$

whereas if $k \geqslant vt$

$$M\frac{d^2u_{k,0}}{dt^2}(t) = \mu(u_{k+1,0}(t) + u_{k-1,0}(t) + u_{k,1}(t) + u_{k,-1}(t) - 4u_{k,0}(t)) + q_k(t). \tag{2.7}$$

Here, q_k is the load applied on the particle with position $(k, 0)$.

Next, (2.1) along with the assumption that the load $q_k(t) = q(\eta)$, allows for transformation of Eqs. (2.5)–(2.7), to

$$Mv^2\frac{d^2u_n}{d\eta^2}(\eta) = \mu(u_n(\eta+1) + u_n(\eta-1) + u_{n+1}(\eta) + u_{n-1}(\eta) - 4u_n(\eta)) \tag{2.8}$$

for $n > 0$, and for $n = 0$

$$v^2\mathfrak{M}(\eta)\frac{d^2u_0}{d\eta^2}(\eta) = \mu(u_0(\eta+1) + u_0(\eta-1) + u_1(\eta) + u_{-1}(\eta) - 4u_0(\eta)) + q(\eta), \tag{2.9}$$

where

$$\mathfrak{M}(\eta) = \begin{cases} M, & \text{for } \eta \geqslant 0, \\ m, & \text{for } \eta < 0. \end{cases} \tag{2.10}$$

2.2.2. Solution for the problem inside the lattice for $n \geqslant 0$

The problem (2.8) and (2.9) is now solved using an approach similar to that presented in Slepyan (2002).

Taking the Fourier transform (outlined in Section 2.1) with respect to η, yields

$$0 = u^F_{n+1} + u^F_{n-1} - 2\Omega_1(\xi, 0 + \mathrm{i}\xi v_*)u^F_n, \quad (n \geqslant 1) \tag{2.11}$$

and

$$(0 + \mathrm{i}\xi v_*)^2 u^F_{0,+} + \beta(0 + \mathrm{i}\xi v_*)^2 u^F_{0,-} = -2(2 - \cos(\xi))u^F_0 + 2u^F_1 + \frac{q^F}{\mu}, \tag{2.12}$$

where $\beta = m/M$, $v_* = \sqrt{M/\mu}\, v$. The symmetry conditions (2.2) about $n = 0$ and the result

$$\left[v^2 \mathfrak{M}(\eta) \frac{d^2 u_0}{d\eta^2}(\eta) \right]^F = M(0 + \mathrm{i}\xi v)^2 u^F_{0,+} + m(0 + \mathrm{i}\xi v)^2 u^F_{0,-}, \tag{2.13}$$

which occurs due to regularisation, have also been used in the derivation of (2.12), (see Appendix A and Chapter 2 of Slepyan, 2002). Here, $0 + \mathrm{i}\xi$ indicates the limit $\lim_{\varepsilon \to +0}(\varepsilon + \mathrm{i}\xi)$, where $0 < \varepsilon \ll 1$ is a regularisation parameter, and in (2.11)

$$\Omega_a(\varkappa, z) = 1 + 2\sin^2(\varkappa/2) + \frac{az^2}{2}. \tag{2.14}$$

The solution, for $n > 0$, is sought in the form

$$u^F_n = \lambda^n u^F_1, \quad (n \geqslant 1), \tag{2.15}$$

where it is required that $|\lambda| \leqslant 1$. After substitution into (2.11), λ can be determined as a solution of

$$\lambda^2 - 2\Omega_1(\xi, 0 + \mathrm{i}\xi v_*)\lambda + 1 = 0. \tag{2.16}$$

Due to the presence of the regularisation parameter in (2.16), the solution can be sought in the form

$$\lambda = \Omega_1(\xi, 0 + \mathrm{i}\xi v_*) - r(\lambda_*)\sqrt{\Omega_1(\xi, 0 + \mathrm{i}\xi v_*)^2 - 1}, \tag{2.17}$$

where

$$\lambda_* = \Omega_1(\xi, 0 + \mathrm{i}\xi v_*) - \sqrt{\Omega_1(\xi, 0 + \mathrm{i}\xi v_*)^2 - 1} \quad \text{and}$$
$$r(z) = \begin{cases} 1 & \text{if } |z| \leqslant 1 \\ -1 & \text{if } |z| > 1. \end{cases}$$

In Section 2.3, when determining the dispersion relations, the regularisation parameter is set to zero and the following form for λ will be useful

$$\lambda = \begin{cases} \Omega_1(\xi, \mathrm{i}\xi v_*) - \mathrm{sign}(\Omega_1(\xi, \mathrm{i}\xi v_*))\sqrt{\Omega_1(\xi, \mathrm{i}\xi v_*)^2 - 1} & \text{for } |\Omega_1(\xi, \mathrm{i}\xi v_*)| > 1, \\ \pm 1 & \text{for } \Omega_1(\xi, \mathrm{i}\xi v_*) = \pm 1, \\ \Omega_1(\xi, \mathrm{i}\xi v_*) \pm \mathrm{i}\sqrt{1 - \Omega_1(\xi, \mathrm{i}\xi v_*)^2} & \text{for } |\Omega_1(\xi, \mathrm{i}\xi v_*)| < 1. \end{cases} \tag{2.18}$$

Next, (2.11) with (2.16) gives the relation $u^F_1 = \lambda u^F_0$. Thus (2.12) gives

$$(0 + \mathrm{i}\xi v_*)^2 u^F_{0,+} + \beta(0 + \mathrm{i}\xi v_*)^2 u^F_{0,-} = 2[\lambda - (2 - \cos(\xi))]u^F_0 + \frac{q^F}{\mu}. \tag{2.19}$$

The alternative to the regularisation outlined in Appendix A, is the use of interface conditions between the defect and the particle adjacent to the defect tip along $n = 0$:

$$mu_0(-0) = Mu_0(+0), \quad m\frac{du_0}{d\eta}(-0) = M\frac{du_0}{d\eta}(+0). \tag{2.20}$$

In other words the suggested regularisation implies the conservation of momentum at the node $(\eta = 0, n = 0)$. Later, it will be shown that for a load corresponding to an energy flux from infinity, the solution to the problem considered here can be constructed and the above conditions will be satisfied.

2.2.3. The Wiener–Hopf equation

Making the additive split (2.4) for u^F_0 in (2.19) provides the Wiener–Hopf equation

$$L(\xi, 0 + \mathrm{i}\xi v_*)u^F_{0,+} + \beta u^F_{0,-} = -\frac{\beta q^F}{2\mu(\lambda - \Omega_\beta(\xi, 0 + \mathrm{i}\xi v_*))}, \tag{2.21}$$

where the kernel function $L(\xi, 0 + \mathrm{i}\xi v_*)$ is given by

$$L(\xi, 0 + \mathrm{i}\xi v_*) = \beta\frac{\lambda - \Omega_1(\xi, 0 + \mathrm{i}\xi v_*)}{\lambda - \Omega_\beta(\xi, 0 + \mathrm{i}\xi v_*)}. \tag{2.22}$$

Note that the above function contains the coefficient β. This ensures that $\lim_{\xi \to \pm\infty} L = 1$, which is a necessary condition for the factorisation of this function in Section 3.

2.3. Dispersion relations for the semi-infinite chain inside the lattice

The zeros and poles of L will now be deduced. They provide information about the dispersion properties for the lattice containing a dynamic semi-infinite chain of particles having a contrast in mass from the ambient lattice. These zeros and poles are found by replacing $0 + \mathrm{i}\xi v_*$ by $\mathrm{i}\omega_*$ and obtaining the expressions for the normalised angular frequency $\omega_* = \sqrt{M/\mu}\,\omega$ for which the numerator and denominator are zero.

Once the zeros and poles of the function L, corresponding to wavenumbers, are identified. the effect of introducing the small regularisation parameter $\varepsilon > 0$ into L will be studied. As in Slepyan (2002), after incorporating the regularisation parameter into L the roots and poles of this function, for a given speed, are then located in the complex plane. The dispersion diagrams will then be used to determine their location following the regularisation (Section 2.4). This information will then be used in Section 3 and Appendix C to solve the Wiener–Hopf equation (2.21).

2.3.1. The zeros of $L(\xi, \mathrm{i}\omega_*)$

Here, by formally setting $\varepsilon = 0$ and $\omega_* = \xi v_*$, the equation

$$\lambda - \Omega_1(\xi, \mathrm{i}\omega_*) = 0, \tag{2.23}$$

must be solved for ω_*. Since it is required that $|\lambda| \leqslant 1$, then the case $|\Omega_1(\xi, \mathrm{i}\omega_*)| > 1$ $(|\lambda| < 1)$ does not provide any solution to the above equation. Therefore, it remains to consider the case $|\lambda| = 1$. Using (2.18), this occurs when $|\Omega_1(\xi, \mathrm{i}\omega_*)| = 1$ or $|\Omega_1(\xi, \mathrm{i}\omega_*)| < 1$. In both situations, referring to (2.16) and (2.18), a solution of (2.23) is also a solution of the equation $\Omega_1(\xi, \mathrm{i}\omega_*) = \pm 1$. It then follows that the roots of $L(\xi, \mathrm{i}\omega_*)$ are

$$\omega^{(1)}_*(\xi) = 2|\sin(\xi/2)|, \quad (\Omega_1(\xi, \mathrm{i}\omega_*) = 1), \tag{2.24}$$

and

$$\omega^{(2)}_*(\xi) = 2\sqrt{1 + \sin^2(\xi/2)}, \quad (\Omega_1(\xi, \mathrm{i}\omega_*) = -1). \tag{2.25}$$

2.3.2. The poles of $L(\xi, \mathrm{i}\omega_*)$

For the poles of $L(\xi, \mathrm{i}\omega_*)$, the solutions of the equation

$$\lambda - \Omega_\beta(\xi, \mathrm{i}\omega_*) = 0 \tag{2.26}$$

are considered. In Colquitt et al. (2013), an infinite line defect contained in a square cell lattice was analysed and (2.26) is also

encountered in that problem. There it was shown, that for $\beta < 1,\ (m < M)$, (2.26) has the solution

$$\omega_*^{(\beta)}(\xi) = \sqrt{\frac{2}{\beta(2-\beta)}\left[1+2\sin^2(\xi/2)+\sqrt{1+4(\beta-1)^2\sin^2(\xi/2)(1+\sin^2(\xi/2))}\right]}. \tag{2.27}$$

The dispersion curves (2.24), (2.25) and (2.27) are given in Figs. 3 and 4, as a function of the dimensionless quantity $\xi a/\pi$ with $a = 1$, in the cases $\beta = 0.1, 0.17, 0.29289$ and 0.7. In both figures, the dispersion relation for the semi-infinite chain (2.24) is represented by the dashed curve, whereas the dispersion curves for ambient lattice are shown as black curves ($\omega_*^{(1)}(\xi) < \omega_*^{(2)}(\xi)$ for all $\xi \in \mathbb{R}$). In each dispersion diagram, the rays $\omega_* = \xi v_*$ are also included for $v_* = 0.25, 0.4, 0.7$, for the purpose of illustration when considering the solution of the Wiener–Hopf equation (2.21) below.

2.4. Description of poles and zeros of L for a given speed

Using the information in Section 2.3, the roots and poles of L for a given speed are now analysed. In particular, the intersection of the line $\omega_* = \xi v_*$ with the dispersion curves will be studied. Each intersection of this line with a dispersion curve indicates a wave generated in the lattice with the frequency and wavenumber corresponding to that intersection point. These waves are supported by either the ambient lattice (in the case of an intersection with the curves given by (2.24) or (2.25)) or the propagating line inclusion (see (2.27)).

For $0 < v_* \leqslant 1$ ($0 < v \leqslant \sqrt{\mu/M}$), the zeros and poles of L are now discussed in detail. In particular, the position of these roots and poles in the complex plane after the regularisation parameter ε is introduced, is also analysed. To do this, it is necessary to introduce the group velocity v_g for waves propagating in the lattice, which is defined by $v_g = d\omega_*/d\xi$, and compare this quantity with the defect speed (see Slepyan, 2002, Chapter 2). In the following, the case when $v_* \neq v_g$ is considered.

If $v_* \leqslant 1$, the function L has one, three or more pairs of simple zeros, associated with the intersections of the ray $\omega_* = \xi v_*$ with $\omega_*^{(1)}(\xi)$ of (2.24), at $\xi \neq 0, \xi = \pm r_1^{(1)}, \pm r_2^{(1)}, \ldots, \pm r_{2z+1}^{(1)}$. For $v_* = 0.4$, this root pattern for $\xi/\pi > 0$ is indicated on Fig. 3(a). Here, the number z decreases as v_* increases, and $z = 0$ for $v_* > v_c^{(1)} \approx 0.2172$. The point $\xi = r_0^{(1)} = 0$ is a removable singularity of L.

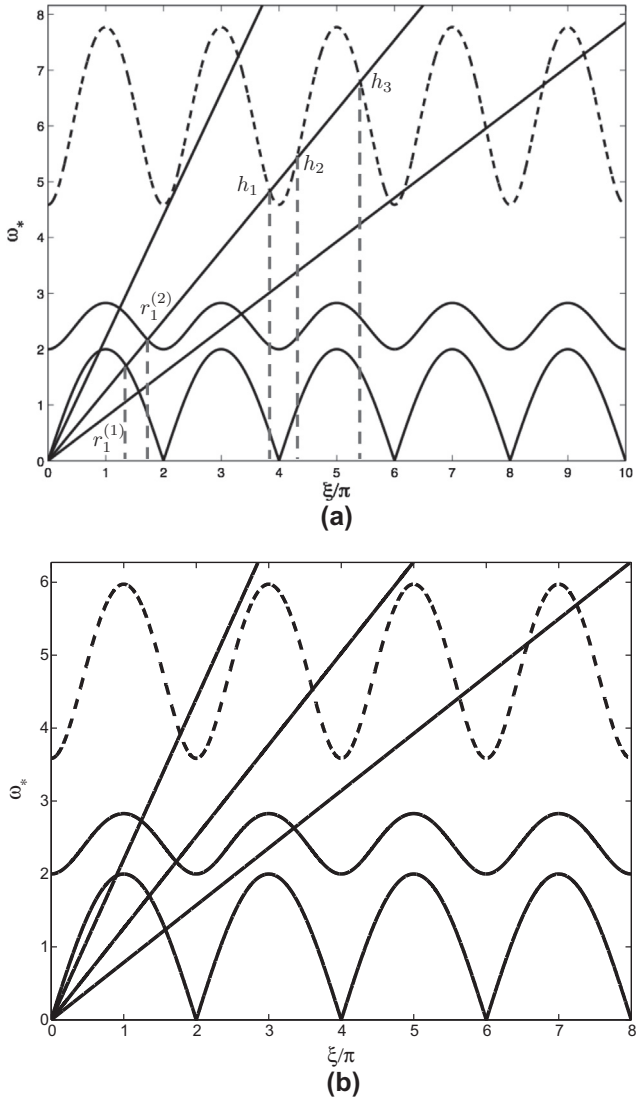

Fig. 3. The dispersion curves (2.24), (2.25) and (2.27) are plotted as functions of the dimensionless quantity $\xi a/\pi$ with $a = 1$, for (a) $\beta = 0.1$ and (b) $\beta = 0.17$. The rays $\omega_* = \xi v_*$ are also shown for the normalised speeds $v_* = 0.25,\ 0.4$ and 0.7.

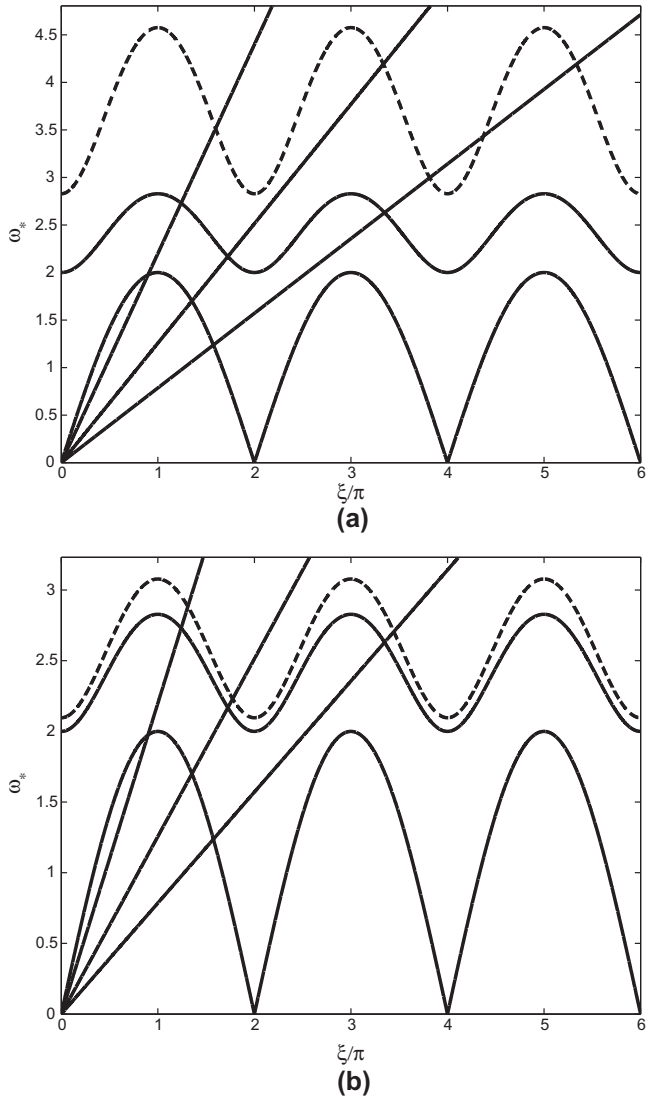

Fig. 4. The dispersion curves (2.24), (2.25) and (2.27) are plotted as functions of the dimensionless quantity $\xi a/\pi$ with $a = 1$, for (a) $\beta = 0.29289$ and (b) $\beta = 0.7$. The rays $\omega_* = \xi v_*$ are also shown for the normalised speeds $v_* = 0.25,\ 0.4$ and 0.7.

The function L also has one, three or more pairs of simple zeros, associated with the intersections of the ray $\omega_* = \xi v_*$ with $\omega_*^{(2)}(\xi)$ of (2.25), at $\xi = \pm r_1^{(2)}, \pm r_2^{(2)}, \ldots, \pm r_{2y+1}^{(2)}$(see Fig. 3(a)). Here, y is non-monotonic for increasing v_*, and $y = 0$ for $v_* > v_c^{(2)} \approx 0.3158$. Also note that $r_{2z+1}^{(1)} < r_1^{(2)}$.

The function L has one, three, or more pairs of simple poles, which correspond to the intersections of the ray $\omega_* = \xi v_*$ and with the pole $\omega_*^{(\beta)}(\xi)$ of (2.27). This occurs at $\xi = \pm h_1, \pm h_2, \ldots, \pm h_{2p+1}$, with p being non-monotonic for v_* increasing (see Fig. 3(a)). Note that $r_{2y+1}^{(2)} < h_1$. If M is fixed and m is allowed to vary, the value of p is also non-monotonic for different β.

For the above mentioned roots and poles of L, for a given speed v_*, the following conditions also hold at the corresponding intersection points of the ray $\omega_* = \xi v_*$ with the dispersion curves:

1. $v_g < v_*$ at
$$\begin{aligned} &\xi = r_{2w-1}^{(1)}, \quad w = 1, \ldots, z+1, \\ &\xi = r_{2a-1}^{(2)}, \quad a = 1, \ldots, y+1, \text{ and} \\ &\xi = h_{2i-1}, \quad i = 1, \ldots, p+1, \end{aligned}$$
2. $v_g > v_*$ at
$$\begin{aligned} &\xi = r_{2w}^{(1)}, \quad w = 1, \ldots, z, \\ &\xi = r_{2a}^{(2)}, \quad a = 1, \ldots, y, \text{ and} \\ &\xi = h_{2i}, \quad i = 1, \ldots, p. \end{aligned}$$

At the intersection points where $v_g > v_*$, when the small regularisation parameter $\varepsilon > 0$ is introduced, these points are then located in the lower half of the complex plane (see Slepyan, 2002). On the other hand, if $v_* > v_g$, after regularisation, the corresponding points will be located in the upper half of the complex plane.

3. The analysis of the Wiener–Hopf equation

In this section, the solution for the Wiener–Hopf equation (2.21) is derived in two steps. Section 3.1 contains properties of the kernel function L and its Cauchy-type factorisation. In Section 3.2, using the information regarding roots and poles of L and a particular choice of the load q that admits an energy flux at infinity, the solution of the Wiener–Hopf equation (2.21) is derived. For the general solution to the Wiener–Hopf equation see Appendix C.

3.1. Properties of the function $L(\xi, 0 + \mathrm{i}\xi v_*)$ and its factorisation

The kernel function $L(\xi, 0 + \mathrm{i}\xi v_*)$ satisfies

$$\mathrm{Re}(L(\xi, 0 + \mathrm{i}\xi v_*)) = \mathrm{Re}(L(-\xi, 0 - \mathrm{i}\xi v_*)),$$

$$\mathrm{Im}(L(\xi, 0 + \mathrm{i}\xi v_*)) = -\mathrm{Im}(L(-\xi, 0 - \mathrm{i}\xi v_*))$$

and so

$$\mathrm{Arg}(L(\xi, 0 + \mathrm{i}\xi v_*)) = -\mathrm{Arg}(L(-\xi, 0 - \mathrm{i}\xi v_*)),$$

where here Arg is the continuous argument of a complex number. That is, if a complex valued function $f : \mathbb{R} \to \mathbb{C}$ defines a contour $\gamma(\xi) = \{z \in \mathbb{C} : \ z = f(t), \ t \in (-\infty, \xi]\}$, then the continuous argument of the function f is

$$\mathrm{Arg}(f(\xi)) = \mathrm{Im}\left[\int_{\{z \in \gamma(\xi)\}} \frac{dz}{z}\right].$$

Additional properties of the kernel function $L(\xi, 0 + \mathrm{i}\xi v_*)$ include:

$$\lim_{|\xi| \to \infty} L(\xi, 0 + \mathrm{i}\xi v_*) = 1,$$

$$\lim_{\xi \to 0} L(\xi, 0 + \mathrm{i}\xi v_*) = \beta. \tag{3.1}$$

The index of L is defined by

$$\begin{aligned} &\mathrm{Ind}(L(\xi, 0 + \mathrm{i}\xi v_*)) \\ &= \frac{1}{2\pi}\left[\lim_{\xi \to \infty} \mathrm{Arg}(L(\xi, 0 + \mathrm{i}\xi v_*)) - \lim_{\xi \to -\infty} \mathrm{Arg}(L(\xi, 0 + \mathrm{i}\xi v_*))\right] \end{aligned} \tag{3.2}$$

and $\mathrm{Ind}(L(\xi, 0 + \mathrm{i}\xi v_*)) = 0$. This is proved in Appendix B.

The function L satisfies the conditions which are necessary for it to be split as a product using the Cauchy-type integral:

$$\begin{aligned} &L = L_+ L_-, \quad L_\pm(\xi, 0 + \mathrm{i}\xi v_*) \\ &= \exp\left(\pm \frac{1}{2\pi \mathrm{i}} \int_{-\infty}^{\infty} \frac{\ln L(s, 0 + \mathrm{i}s v_*)}{s - \xi} ds\right), \quad \pm \mathrm{Im}\xi > 0, \end{aligned} \tag{3.3}$$

where '–' ('+') denotes the function analytic in the lower (upper) half of the complex plane. Then (2.21) is written as

$$L_+ u_{0,+}^F + \frac{\beta u_{0,-}^F}{L_-} = \frac{\beta q^F}{2\mu L_-(\lambda - \Omega_\beta(\xi, 0 + \mathrm{i}\xi v_*))}. \tag{3.4}$$

From (2.22), the Wiener–Hopf equation (2.21) also takes the form:

$$L_+ u_{0,+}^F + \frac{\beta u_{0,-}^F}{L_-} = \frac{\beta - L}{2\mu L_-(1 - \beta)(0 + \mathrm{i}\xi v_*)^2} q^F. \tag{3.5}$$

3.2. Additive split of the right-hand side of (3.4)

The function q is chosen in such a way that it allows for the additive split of the right-hand side of (3.4) into + and − functions. This is carried out by assuming energy is supplied to the mass at $n = 0, \ \eta = 0$, by a feeding wave at infinity. This approach, applied in Slepyan (2001a, 2002), results in the appearance of the regularised Dirac delta function in the right-hand side of (3.4), which allows for a straight-forward additive split. In what follows, the additive split is carried out for the point $\xi = 0$, for the general case when all singular points of the right-hand side of (3.4) are considered, see Appendix C.

According to Chapter 2 of Slepyan (2002), the function $u_0(\eta)$ can be obtained from a sum of residues which correspond to the singular points of the integral kernel of the inverse Fourier transform of $u_{0,\pm}^F$. For this reason, behaviour of the term

$$\frac{1}{L_-(\lambda - \Omega_\beta(\xi, 0 + \mathrm{i}\xi v_*))}, \tag{3.6}$$

in the right-hand side of (3.4) near the point $\xi = 0$ is now considered. As mentioned in Section 2.4, the function L has a removable singularity at $\xi = 0$, and so L_- is also bounded in the vicinity of this point. However, $\xi = 0$ is a zero of the expression (2.26), which results in singular behaviour in the right-hand side of (3.4).

Let the load q have the form

$$q(\eta) = A_0^{(1)} 2\varepsilon \exp(\varepsilon\eta) H(-\eta), \tag{3.7}$$

so that $q_+^F = 0$, and

$$q_-^F = \frac{2\varepsilon A_0^{(1)}}{(\varepsilon + \mathrm{i}\xi)}.$$

Here $\varepsilon > 0$ is treated as a regularisation parameter and the overall force applied along the defect is independent of ε. Formally, the regularisation parameter can be considered as complex and its non-zero imaginary part would lead to oscillatory behaviour of the load q. In the current paper, we assume ε is real and positive and hence q decays exponential as $\eta \to -\infty$ with no oscillation.

Note that $\lim_{\varepsilon \to +0} q = 0$. The root $\xi = 0$ of the denominator in (3.6) (when $\varepsilon = 0$) is a point where $v_* < v_g$ for $v_* < 1$ (see Figs. 3 and 4). Therefore, this point is located in the lower half of the

complex plane when the regularisation parameter $\varepsilon > 0$ is introduced. Since

$$L(\xi, 0 + i\xi v_*) \sim \beta - \frac{\beta(1-\beta)v_*^2}{2\sqrt{1-v_*^2}}\xi + O(\xi^2), \quad \text{for } \xi \to 0,$$

then this together with (3.7) in (3.5), leads to

$$L_+ u_{0,+}^F + \frac{\beta u_{0,-}^F}{L_-} = D_0 \lim_{\varepsilon \to +0} \frac{2\varepsilon}{(\varepsilon + i\xi)(\varepsilon - i\xi)} = 2\pi D_0 \delta(\xi) = D_0\left[\frac{1}{0+i\xi} + \frac{1}{0-i\xi}\right], \tag{3.8}$$

where

$$D_0 = -\frac{iA_0^{(1)}\beta^{1/2}}{4\mu\sqrt{1-v_*^2}} \exp\left(\frac{1}{\pi}\int_0^\infty \frac{\text{Arg}(L(s, 0 + is v_*))}{s} ds\right). \tag{3.9}$$

Here, the result

$$\lim_{\xi \to 0} L_\pm(\xi, 0 + i\xi v_*) = \beta^{1/2} \exp\left(\pm\frac{1}{\pi}\int_0^\infty \frac{\text{Arg}(L(s, 0 + is v_*))}{s} ds\right) \tag{3.10}$$

has been used (which follows from (3.1) and (3.3)).

Unlike the problem for a propagating crack within the lattice, here the kernel $L(\xi, 0 + i\xi v_*)$ is bounded for small wavenumbers tending to zero. In the problem for the crack, the kernel L exhibits singular behaviour which is $O(\xi^{-1})$. Consequently this leads to the square root singular behaviour of the functions $L_\pm$ (see Slepyan, 2001a,c). It is possible to find other examples of problems of the current type where bounded behaviour of L in the vicinity of the zero wavenumber as in (3.10) is observed, for instance, Slepyan and Ayzenberg-Stepanenko (2004) includes the propagation of an inclusion that consists of bonds with contrasting stiffness from the ambient square or triangular lattice.

From (3.8) it then follows

$$u_{0,+}^F = \frac{D_0}{L_+}\frac{1}{0-i\xi}, \quad u_{0,-}^F = \frac{D_0 L_-}{\beta}\frac{1}{0+i\xi}. \tag{3.11}$$

In terms of the moving coordinate system, the function $u_0(\eta)$ can be defined through

$$u_0 = u_0^+ + u_0^-, \tag{3.12}$$

where the terms $u_0^\pm$ are given by

$$u_0^+ = \frac{1}{2\pi}\int_{-\infty}^0 u_0^F(\xi) e^{-i\xi\eta} d\xi, \quad \text{Im}(\eta) > 0, \tag{3.13}$$

$$u_0^- = \frac{1}{2\pi}\int_0^\infty u_0^F(\xi) e^{-i\xi\eta} d\xi, \quad \text{Im}(\eta) < 0, \tag{3.14}$$

where $\text{Im}(\eta)$ in both cases is treated as a small regularisation parameter and the function u_0^F is given by the sum of the functions in (3.11) (see Slepyan, 2002).

4. Physical applicability of the model and concluding remarks

For the load of the form (3.7), the displacements at the defect tip and at infinity are compared.

According to Slepyan (2002, Chapter 2), the formulae relating these expressions to displacements at the defect tip and far away from the tip along the defect are

$$u_0(-0) = \lim_{p\to\infty} p u_{0,-}^F(-ip), \quad u_0(-\infty) = \lim_{p\to+0} p u_{0,-}^F(-ip).$$

Along with (3.10) and (3.11), these limits lead to

$$u_0(-\infty) = \frac{D_0}{\beta^{1/2}} \exp\left(-\frac{1}{\pi}\int_0^\infty \frac{\text{Arg}(L(s, 0 + is v_*))}{s} ds\right) \quad \text{and} \quad u_0(-0) = \frac{D_0}{\beta}. \tag{4.1}$$

Also, the relations

$$u_0(+0) = \lim_{p\to\infty} p u_{0,+}^F(ip)$$

and

$$\frac{du_0}{d\eta}(+0) = \lim_{p\to\infty} p[p u_{0,+}^F(ip) - u_0(+0)],$$

$$\frac{du_0}{d\eta}(-0) = \lim_{p\to\infty} p[u_0(-0) - p u_{0,-}^F(-ip)]$$

are valid, and they lead to the formulae

$$u_0(+0) = D_0, \quad \frac{du_0}{d\eta}(-0) = \frac{du_0}{d\eta}(+0) = 0.$$

Recalling $\beta = m/M$, together with the preceding limits and (4.1), it can be shown that conditions (2.20) will be satisfied.

Therefore, according to (4.1) the ratio of the tip displacement to the displacement along the defect in the far-field is

$$\frac{u_0(-0)}{u_0(-\infty)} = \beta^{-1/2} \exp\left(\frac{1}{\pi}\int_0^\infty \frac{\text{Arg}(L(s, 0 + is v_*))}{s} ds\right).$$

This quantity is plotted for $0 \leqslant v_* \leqslant 1$ in Fig. 5, for the parameters $\beta = 0.1, 0.175, 0.25, 0.5$, and 0.75. For low speeds, $u_0(-0)/u_0(-\infty)$ behaves non-monotonically and gives a non-smooth behaviour for v_* tending to 0 (see Fig. 5). For these low values of speed, there occur many intersections of the ray $\omega = \xi v_*$ with the dispersion curves in Figs. 3 and 4, causing the function Arg L to oscillate rapidly and generate this non-smooth behaviour. Those values of v_*, which produce the non-monotonic behaviour, can be linked to the region of instability of the model which has been studied through the notion of energy dissipation of cracks and inclusions propagating through lattices (Slepyan, 2002; Slepyan and Ayzenberg-Stepanenko, 2004). Note that, as the value of the mass contrast parameter decreases, the range of speeds for which we have this non-monotonic behaviour increases. In the study of the energy dissipation, due to a crack growing through lattices (Slepyan, 2002), speed regimes giving rise to non-monotonic behaviour of the energy indicate that, at those speeds, the models do not describe the physical situation of the defect moving through the lattice accurately.

The ratio $u_0(-0)/u_0(-\infty)$, also appears to tend to a finite value for $v_* \to 0$ (the case of a stationary defect). Indeed, since formally setting $v_* = 0$, it follows from (2.14) that $\Omega_\beta(\xi, 0 + i\xi v^*)|_{v_*=0} \approx \Omega_1(\xi, 0 + i\xi v^*)|_{v_*=0}$ (which are approximately equal due to the presence of the small regularisation parameter), and then $L \approx 1$ so Arg $L \approx 0$. In this case $u_0(-0)/u_0(-\infty) \approx \beta^{-1/2}$.

For larger values of v_*, after the ratio $u_0(-0)/u_0(-\infty)$ attains its minimum value in the region $0 < v_* \leqslant 1$, a smooth monotonic increase can be observed as the ratio tends to a finite value for $v_* \to 1$. A similar feature was also observed in the analysis of the energy release rate of a crack within a lattice. This occurs for large crack speeds and in this region the model describes the propagation of a crack through the lattice (Slepyan, 2002). It can also be concluded that the larger the value of β (i.e. the closer the lattice approaches the case of a homogeneous lattice), the smaller the effect of the mass contrast parameter on the ratio $u_0(-0)/u_0(-\infty)$, as expected. Here, a simple calculation shows that for $\beta \to 1$, from (2.22), $L \to 1$. Therefore, when $\beta \to 1, u_0(-0)/u_0(-\infty) \to 1$ for $0 < v_* \leqslant 1$. This trend can be seen in Fig. 5, for increasing β.

Note that $u_0(-0)/u_0(-\infty)$ is always greater than 1, for all $0 \leqslant v_* \leqslant 1$ and for each value of β, which implies the displacement

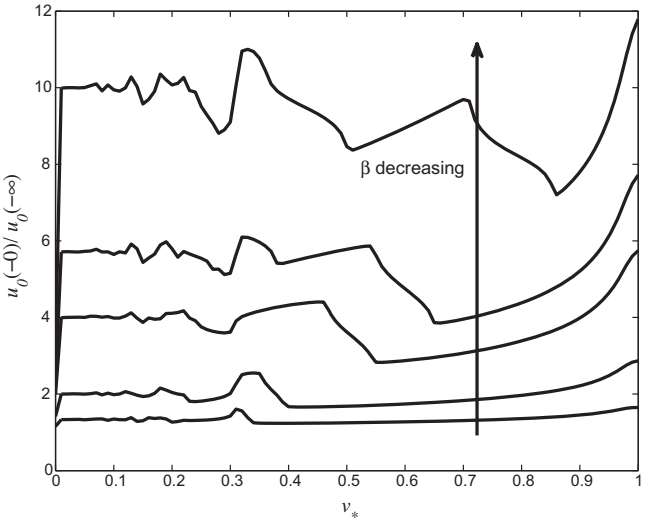

Fig. 5. The ratio $u_0(-0)/u_0(-\infty)$ plotted as a function of the normalised defect speed v_*, for $\beta = 0.1, 0.175, 0.25, 0.5$, and 0.75.

associated with the defect tip is always greater than the displacement along this defect at infinity. In Slepyan (2002), energy dissipation due to a crack propagating through a lattice structure was considered, where, when a bond is broken along the line of the crack in the lattice, energy is released in the form of dissipative waves which carry energy from the crack tip into the lattice. In the present paper, instead of a propagating crack in the lattice, the situation when there is a propagating inclusion is considered. Hence, when the particle of mass m at $\eta = 0,\ n = 0$ undergoes a phase transition, energy is released not only into the ambient lattice as part of this dissipation, but also energy will be channelled along the inclusion, acting as a waveguide. Localised modes within this inclusion are generated for frequencies outside the ambient lattice stop band defined by $\omega^2 > 8$. This is depicted in Figs. 3 and 4 (the dashed line is the dispersion curve for the inclusion). From this, in order for these localised modes to be generated, it is seen that the inclusion is needed to propagate at higher speeds. Hence, this explains the behaviour of the defect tip displacement in comparison to the displacements at infinity along this inclusion for higher speeds.

Here, the solution for the problem of the propagating line defect inside a square lattice has been presented for a particular choice of the load q. An advantage of the model is that it allows for the dispersive nature of the lattice to be studied as dispersion relations can be obtained explicitly. The influence of the speed of the defect and its effect on the wave dispersion can also be considered. This is one of the most valuable features of lattice models in general and examples of other problems where these features are discussed include Slepyan (2001a) and Slepyan and Ayzenberg-Stepanenko (2004). An important aspect of the problem presented here, is that the lattice allows for localisation of waves along the defect, due to the defect having smaller density than the ambient lattice.

Models for propagating defects within lattices considered in, for instance Slepyan (2001a,c), also allow for the prediction of ranges of defect speeds for which the models make physical sense. In Slepyan (2001a,c), this was carried out through the analysis of the energy characteristics of the propagating defects. This can usually be predicted by observing smooth monotonic behaviour in the solution for a range of defect speeds. Here, there is also such behaviour, and the influence of the mass contrast parameter on this range of speeds can be determined.

Acknowledgements

The authors would like to acknowledge the financial support of the UK Engineering and Physical Sciences Research Council through the research Grants EP/H018239/1 and EP/H018514/1. A.B.M also gratefully acknowledges the financial support from research Grant PIAP-GA-2011-286110-INTERCER2.

Appendix A. The regularisation (2.13)

Consider the inertia term

$$v^2 \mathfrak{M}(\eta) \frac{d^2 u_0}{d\eta^2}(\eta),$$

which appears in (2.9) for the equation of motion along $n = 0$. Applying the Fourier transform of this term gives

$$\begin{aligned} & v^2 \int_{-\infty}^{\infty} \mathfrak{M}(\eta) \frac{d^2 u_0}{d\eta^2}(\eta) e^{i\xi\eta} d\eta \\ & = v^2 \left\{ \lim_{\sigma \to 0} \left[\int_0^{\infty} M \frac{d^2 u_0^+}{d\eta^2}(\eta) e^{i(\xi + i\sigma)\eta} d\eta + \int_{-\infty}^{0} m \frac{d^2 u_0^-}{d\eta^2}(\eta) e^{i(\xi - i\sigma)\eta} d\eta \right] \right\} \\ & = v^2 \left\{ \lim_{\substack{b \to 0 \\ \sigma \to 0}} \left[\int_{-b}^{\infty} M \frac{d^2 u_0^+}{d\eta^2}(\eta) e^{i(\xi + i\sigma)\eta} d\eta + \int_{-\infty}^{b} m \frac{d^2 u_0^-}{d\eta^2}(\eta) e^{i(\xi - i\sigma)\eta} d\eta \right] \right\}, \end{aligned} \tag{A.1}$$

where the definition of $\mathfrak{M}$ in (2.10) and the split (2.3) have been used. Also it is assumed in these integrals σ is positive, in accordance with Section 2.1, so that the integrals converge.

Owing to integration by parts

$$\int_{-b}^{\infty} \frac{d^2 u_0^+}{d\eta^2}(\eta) e^{i(\xi + i\sigma)\eta} d\eta = \left[\frac{du_0^+}{d\eta}(\eta) e^{i(\xi + i\sigma)\eta} \right]_{-b}^{\infty} - (-\sigma + i\xi) \left[u_0^+(\eta) e^{i(\xi + i\sigma)\eta} \right]_{-b}^{\infty} + (-\sigma + i\xi)^2 \int_{-b}^{\infty} u_0^+(\eta) e^{i(\xi + i\sigma)\eta} d\eta.$$

Next, using the fact that the support of u^+ is $\{\eta : \eta \geqslant 0\}$, this reduces to

$$\int_{-b}^{\infty} \frac{d^2 u_0^+}{d\eta^2}(\eta) e^{i(\xi + i\sigma)\eta} d\eta = (-\sigma + i\xi)^2 \int_{-b}^{\infty} u_0^+(\eta) e^{i(\xi + i\sigma)\eta} d\eta. \tag{A.2}$$

Similarly, it can be shown

$$\int_{-\infty}^{b} \frac{d^2 u_0^-}{d\eta^2}(\eta) e^{i(\xi - i\sigma)\eta} d\eta = (\sigma + i\xi)^2 \int_{-\infty}^{b} u_0^-(\eta) e^{i(\xi - i\sigma)\eta} d\eta. \tag{A.3}$$

Combining (A.2) and (A.3) with (A.1) and allowing σ to tend to zero, yields

$$v^2 \int_{-\infty}^{\infty} \mathfrak{M}(\eta) \frac{d^2 u_0}{d\eta^2}(\eta) e^{i\xi\eta} d\eta = M(0 + i\xi v)^2 u_{0,+}^F + m(0 + i\xi v)^2 u_{0,-}^F,$$

which is (2.13).

Appendix B. Evaluation of the index of L

In this section, it is shown that

$$\mathrm{Ind}(L(\xi, 0 + i\xi v_*)) = 0.$$

First, from the definition (3.2) of the index of L, if the function L can be written as a product

$$L(\xi, 0 + i\xi v_*) = \prod_{j=1}^{N} L_j(\xi, 0 + i\xi v_*), \tag{B.1}$$

then

$$\mathrm{Ind}(L(\xi,0+\mathrm{i}\xi v_*)) = \sum_{j=1}^{N}\mathrm{Ind}(L_j(\xi,0+\mathrm{i}\xi v_*)) \tag{B.2}$$

and in order to prove the index of L is zero, the same property needs to proved for the sum in the right-hand side of (B.2).

B.1. Auxiliary functions

Let

$$\begin{aligned}\sigma_a(\xi,0+\mathrm{i}\xi v_*) &= \sqrt{4\sin^2(\xi/2)+a(0+\mathrm{i}\xi v_*)^2},\\ \tau_a(\xi,0+\mathrm{i}\xi v_*) &= \sqrt{(\sigma_a(\xi,0+\mathrm{i}\xi v_*))^2+4}.\end{aligned} \tag{B.3}$$

Then with (2.14) and (2.17), the following relations hold

$$\begin{aligned}(\sigma_a(\xi,0+\mathrm{i}\xi v_*))^2+2 &= 2\Omega_a(\xi,0+\mathrm{i}\xi v_*),\\ (\tau_a(\xi,0+\mathrm{i}\xi v_*))^2 &= 2(\Omega_a(\xi,0+\mathrm{i}\xi v_*)+1),\end{aligned} \tag{B.4}$$

$$\lambda(\xi,0+\mathrm{i}\xi v_*) = \frac{\tau_1(\xi,0+\mathrm{i}\xi v_*)-\sigma_1(\xi,0+\mathrm{i}\xi v_*)}{\tau_1(\xi,0+\mathrm{i}\xi v_*)+\sigma_1(\xi,0+\mathrm{i}\xi v_*)}. \tag{B.5}$$

From (2.14) and (B.4)

$$\begin{aligned}-\pi &< \arg[(\sigma_a(\xi,0+\mathrm{i}\xi v_*))^2] < \pi,\\ -\pi &< \arg[(\tau_a(\xi,0+\mathrm{i}\xi v_*))^2] < \pi\end{aligned}$$

and so

$$\begin{aligned}-\pi/2 &< \arg[\sigma_a(\xi,0+\mathrm{i}\xi v_*)] < \pi/2,\\ -\pi/2 &< \arg[\tau_a(\xi,0+\mathrm{i}\xi v_*)] < \pi/2,\end{aligned} \tag{B.6}$$

with

$$\mathrm{Re}(\sigma_a(\xi,0+\mathrm{i}\xi v_*))>0, \quad \mathrm{Re}(\tau_a(\xi,0+\mathrm{i}\xi v_*))>0. \tag{B.7}$$

Here arg denotes the principle argument, where for $z\in\mathbb{C}$, $-\pi < \arg(z) \leqslant \pi$.

Also note that (2.14) and (B.4) give

$$\mathrm{sign}[\mathrm{Im}(\sigma_a(\xi,0+\mathrm{i}\xi v_*))] = \mathrm{sign}[\mathrm{Im}(\tau_a(\xi,0+\mathrm{i}\xi v_*))]. \tag{B.8}$$

Then (B.7), (B.8) and (B.5) imply that λ satisfies $|\lambda|\leqslant 1$.

B.2. Alternate representation for L

Combining (B.4) and (B.5) and (2.22), an alternative representation for L has the form

$$L(\xi,0+\mathrm{i}\xi v_*) = \beta\frac{C(\xi,0+\mathrm{i}\xi v_*)}{D_\beta(\xi,0+\mathrm{i}\xi v_*)} \tag{B.9}$$

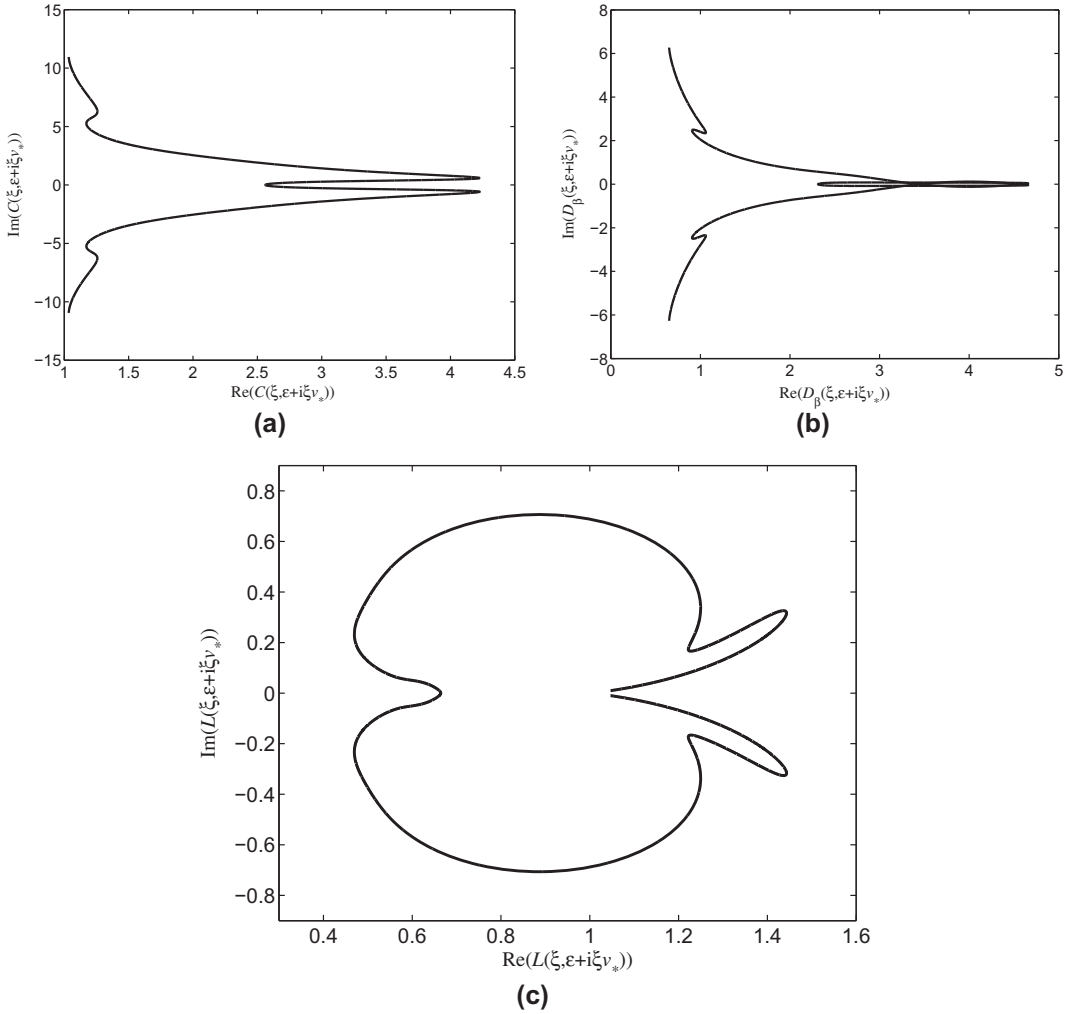

Fig. 6. Plot of the real part against the imaginary part of the functions (a) $C(\xi,\varepsilon+\mathrm{i}\xi v_*)$, (b) $D_\beta(\xi,\varepsilon+\mathrm{i}\xi v_*)$, of (B.10), and (c) $L(\xi,\varepsilon+\mathrm{i}\xi v_*)$ in (B.9). The plots are given for $\xi\in[-4\pi,4\pi]$, $\beta=0.6$, $v_*=0.45$ and $\varepsilon=0.5$.

with

$$C(\xi,0+\mathrm{i}\xi v_*)=\sigma_1(\xi,0+\mathrm{i}\xi v_*)+\tau_1(\xi,0+\mathrm{i}\xi v_*),$$
$$D_\beta(\xi,0+\mathrm{i}\xi v_*)=\frac{(\sigma_\beta(\xi,0+\mathrm{i}\xi v_*))^2}{\sigma_1(\xi,0+\mathrm{i}\xi v_*)}+\frac{(\tau_\beta(\xi,0+\mathrm{i}\xi v_*))^2}{\tau_1(\xi,0+\mathrm{i}\xi v_*)}. \tag{B.10}$$

B.3. Index of the function $C(\xi,0+\mathrm{i}\xi v_*)$

Owing to (B.6)–(B.8),

$$-\pi/2<\arg\left[C(\xi,0+\mathrm{i}\xi v_*)\right]<\pi/2,\quad \text{for } \xi\in\mathbb{R}, \tag{B.11}$$

$$|C(\xi,0+\mathrm{i}\xi v_*)|>0, \tag{B.12}$$

implying

$$\mathrm{Ind}(C(\xi,0+\mathrm{i}\xi v_*))=0. \tag{B.13}$$

B.4. Index of the function $D_\beta(\xi,0+\mathrm{i}\xi v_*)$

Since $0<\beta<1$,

$$\arg[\sigma_\beta(\xi,0+\mathrm{i}\xi v_*)]\leqslant\arg[\sigma_1(\xi,0+\mathrm{i}\xi v_*)]\quad \text{for } \xi\geqslant 0.$$

Therefore,

$$-\pi/2<\arg\left[\frac{\sigma_\beta(\xi,0+\mathrm{i}\xi v_*)}{\sigma_1(\xi,0+\mathrm{i}\xi v_*)}\right]\leqslant 0,\quad \text{for } \xi\geqslant 0$$

and so

$$-\pi/2<\arg\left[\frac{(\sigma_\beta(\xi,0+\mathrm{i}\xi v_*))^2}{\sigma_1(\xi,0+\mathrm{i}\xi v_*)}\right]<\pi/2,\quad \text{for } \xi\geqslant 0.$$

Similar reasoning allows for this inequality to be extended to the case $\xi\in\mathbb{R}$, and also leads to the inequality

$$-\pi/2<\arg\left[\frac{(\tau_\beta(\xi,0+\mathrm{i}\xi v_*))^2}{\tau_1(\xi,0+\mathrm{i}\xi v_*)}\right]<\pi/2,\quad \text{for } \xi\in\mathbb{R}.$$

Thus for $0<\beta<1$

$$-\pi/2<\arg\left[D_\beta(\xi,0+\mathrm{i}\xi v_*)\right]<\pi/2,\quad \text{for } \xi\in\mathbb{R} \tag{B.14}$$

and due to (B.7)

$$|D_\beta(\xi,0+\mathrm{i}\xi v_*)|>0. \tag{B.15}$$

These facts give rise to

$$\mathrm{Ind}(D_\beta(\xi,0+\mathrm{i}\xi v_*))=0.$$

B.5. Index of the function $L(\xi,0+\mathrm{i}\xi v_*)$

Finally, this along with (B.1), (B.2) and (B.13) yields

$$\mathrm{Ind}(L(\xi,0+\mathrm{i}\xi v_*))=0. \tag{B.16}$$

As an example, the plot of the functions $C(\xi,0+\mathrm{i}\xi v_*)$, $D_\beta(\xi,0+\mathrm{i}\xi v_*)$, $L(\xi,0+\mathrm{i}\xi v_*)$ are given in Fig. 6. In particular, for the chosen parameter values, Fig. 6(a) and (b) satisfy the conditions (B.11) and (B.12); and (B.14) and (B.15) are satisfied, respectively. Also the plot Fig. 6(c) shows the path L traces in the complex plane for $\xi\in[-4\pi,4\pi]$. It can be seen that this contour in the complex plane does not contain or pass through the origin, which is predicted by (B.16).

Appendix C. An extended class of right-hand sides in the Wiener–Hopf equation (3.4)

In this section, the general procedure for solving the Wiener–Hopf equation (3.4) is described. By linear superposition, it will be shown below that (3.4) can be written in the form

$$\begin{aligned}L_+u^F_{0,+}+\frac{\beta u^F_{0,-}}{L_-}=-\frac{\beta}{\mu}\Bigg(&\mathcal{A}_0\left[\frac{1}{0+\mathrm{i}\xi}+\frac{1}{0-\mathrm{i}\xi}\right]\\&+\sum_{w=1}^{z+1}\left\{\mathcal{A}_w^{(+)}\left[\frac{1}{0+\mathrm{i}(\xi-r^{(1)}_{2w-1})}+\frac{1}{0-\mathrm{i}(\xi-r^{(1)}_{2w-1})}\right]\right.\\&\left.+\mathcal{A}_w^{(-)}\left[\frac{1}{0+\mathrm{i}(\xi+r^{(1)}_{2w-1})}+\frac{1}{0-\mathrm{i}(\xi+r^{(1)}_{2w-1})}\right]\right\}\\&+\sum_{q=1}^{y+1}\left\{\mathcal{B}_q^{(+)}\left[\frac{1}{0+\mathrm{i}(\xi-r^{(2)}_{2q-1})}+\frac{1}{0-\mathrm{i}(\xi-r^{(2)}_{2q-1})}\right]\right.\\&\left.+\mathcal{B}_q^{(-)}\left[\frac{1}{0+\mathrm{i}(\xi+r^{(2)}_{2q-1})}+\frac{1}{0-\mathrm{i}(\xi+r^{(2)}_{2q-1})}\right]\right\}\\&+\sum_{i=1}^{p}\left\{\mathcal{C}_i^{(+)}\left[\frac{1}{0+\mathrm{i}(\xi-h_{2i})}+\frac{1}{0-\mathrm{i}(\xi-h_{2i})}\right]\right.\\&\left.+\mathcal{C}_i^{(-)}\left[\frac{1}{0+\mathrm{i}(\xi+h_{2i})}+\frac{1}{0-\mathrm{i}(\xi+h_{2i})}\right]\right\}\Bigg),\end{aligned} \tag{C.1}$$

where the numbers p, z, and y depend on the normalised speed v_* and $\mathcal{A}_0=-\mu D_0/\beta$ (see (3.9)). Note that the required split for the right-hand side into '+' and '−' functions is achieved in the above equation.

In order to factorise the right-hand side of (3.4), the singular points must be identified. Non-trivial solutions of (3.4), correspond to the poles of (3.6), which according to the Section 2.4, occur for the wavenumbers $\xi=r^{(1)}_{2w-1},r^{(2)}_{2q-1},\ h_{2i}$ for $w=1,\ldots,z+1, q=1,\ldots,y+1$ and $i=1,\ldots,p$. Note that the wavenumbers $\xi=h_{2i-1}$ for $i=1,\ldots,p+1$, are removable singularities of the right-hand side of (3.4), since they appear as roots of

$$\lambda-\Omega_\beta(\xi,0+\mathrm{i}\xi v_*)=0, \tag{C.2}$$

when $\varepsilon=0$ and on the dispersion diagram $v_*>v_g$ at these points, implying that these are poles of L_- located in the upper half of the complex plane.

In addition to the singular points of (3.6), it is important to mention that while the point $\xi=r^{(1)}=0$ is a removable singularity of the function L, it is a singular point of (3.6), since it is root of (C.2) when $\varepsilon=0$. This case was already treated in Section 3.

Asymptotes of (3.6) near singular points and choices for the external load q: As mentioned in Section 3.2, the function $u_0(t)$ will be represented as a sum of residues which correspond to the singular points of the integral kernel of the inverse Fourier transform of $u^F_{0,\pm}$. For this reason, behaviour of the right-hand side of (3.4) near singular points of (3.6) is now considered, and appropriate choices of the function $q(\eta)$ will also be given.

(i) In the vicinity of the singularity of $1/L_-$ at $\xi=r^{(1)}_{2w-1}$, the function in (3.6) has the asymptotic representation

$$\frac{1}{L_-(\lambda-\Omega_\beta(\xi,0+\mathrm{i}\xi v_*))}\sim\frac{C^{(1)}_{2w-1}}{\sqrt{0+\mathrm{i}(\xi-r^{(1)}_{2w-1})}}. \tag{C.3}$$

Now consider the external load

$$q=A^{(1)}_{2w-1}\sqrt{2\varepsilon}\exp\left(-\{\varepsilon+\mathrm{i}r^{(1)}_{2w-1}\}\eta\right)H(\eta),$$

with $A^{(1)}_{2w-1}$ being the intensity of the load, so that

$$q^F = A^{(1)}_{2w-1}\frac{\sqrt{2\varepsilon}}{\varepsilon - \mathrm{i}(\xi - r^{(1)}_{2w-1})}.$$

This, along with (C.3) in (3.4) gives

$$\begin{aligned} L_+u^F_{0,+} + \frac{\beta u^F_{0,-}}{L_-} &= -\frac{\beta A^{(1)}_{2w-1}C^{(1)}_{2w-1}}{2\mu}\lim_{\varepsilon\to+0}\frac{\sqrt{2\varepsilon}}{(\varepsilon - \mathrm{i}(\xi - r^{(1)}_{2w-1}))\sqrt{\varepsilon + \mathrm{i}(\xi - r^{(1)}_{2w-1})}} \\ &= -\frac{\beta A^{(1)}_{2w-1}C^{(1)}_{2w-1}}{\mu}\pi\delta(\xi - r^{(1)}_{2w-1}). \end{aligned}$$

In connection with the limit above, see Slepyan (2002, Chapter 2). The additive split can now be achieved through the Dirac delta function, so that

$$L_+u^F_{0,+} + \frac{\beta u^F_{0,-}}{L_-} = -\frac{\beta A^{(1)}_{2w-1}C^{(1)}_{2w-1}}{2\mu}\left[\frac{1}{0 + \mathrm{i}(\xi - r^{(1)}_{2w-1})} + \frac{1}{0 - \mathrm{i}(\xi - r^{(1)}_{2w-1})}\right].$$

(ii) A similar additive split can also be made when considering the wavenumbers $\xi = r^{(2)}_{2q-1}$, $q = 1,\ldots,y+1$, where now in the vicinity of $\xi = r^{(2)}_{2q-1}$,

$$\frac{1}{L_-(\lambda - \Omega_\beta(\xi, 0 + \mathrm{i}\xi v_*))} \sim \frac{C^{(2)}_{2q-1}}{\sqrt{0 + \mathrm{i}(\xi - r^{(2)}_{2q-1})}}$$

and the external load

$$q = A^{(2)}_{2q-1}\sqrt{2\varepsilon}\exp\left(-\left\{\varepsilon + \mathrm{i}r^{(2)}_{2q-1}\right\}\eta\right)H(\eta)$$

should be considered.

(iii) For ξ in the vicinity of the singularities h_{2i}, $i = 1,\ldots,p$,

$$\frac{1}{L_-(\lambda - \Omega_\beta(\xi, 0 + \mathrm{i}\xi v_*))} \sim \frac{C_{2i}}{0 - \mathrm{i}(\xi - h_{2i})}$$

and if the q is chosen as

$$q = 2\varepsilon B_{2i}\exp(\{\varepsilon - \mathrm{i}h_{2i}\}\eta)H(-\eta)$$

with

$$q^F = \frac{2\varepsilon B_{2i}}{\varepsilon + \mathrm{i}(\xi - h_{2i})},$$

then the Wiener–Hopf equation (3.4) takes the form

$$\begin{aligned} L_+u^F_{0,+} + \frac{\beta u^F_{0,-}}{L_-} &= -\frac{\beta B_{2i}C_{2i}}{2\mu}\lim_{\varepsilon\to+0}\frac{2\varepsilon}{(\varepsilon - \mathrm{i}(\xi - h_{2i}))(\varepsilon + \mathrm{i}(\xi - h_{2i}))} \\ &= -\frac{\beta B_{2i}C_{2i}}{\mu}\pi\delta(\xi - h_{2i}) \\ &= -\frac{\beta B_{2i}C_{2i}}{2\mu}\left[\frac{1}{0 + \mathrm{i}(\xi - h_{2i})} + \frac{1}{0 - \mathrm{i}(\xi - h_{2i})}\right]. \end{aligned}$$

Note that for the wavenumbers $\xi = -r^{(1)}_{2w-1}$, $-r^{(2)}_{2q-1}$, and $-h_{2i}$ a similar split of the right-hand side of (3.4) can be made to that described in (i)–(iii) above.

Consulting parts (i)–(iii) above and by applying an argument of linear superposition with Eq. (3.4), Eq. (C.1) is derived.

C.1. The solution of the Wiener–Hopf equation

The solution of (C.1) is then

$$\begin{aligned} u^F_{0,+} = -\frac{\beta}{\mu L_+}\Bigg(&\sum_{w=1}^{z+1}\left\{\frac{\mathcal{A}^{(+)}_w}{0 - \mathrm{i}(\xi - r^{(1)}_{2w-1})} + \frac{\mathcal{A}^{(-)}_w}{0 - \mathrm{i}(\xi + r^{(1)}_{2w-1})}\right\} \\ &+\sum_{q=1}^{y+1}\left\{\frac{\mathcal{B}^{(+)}_q}{0 - \mathrm{i}(\xi - r^{(2)}_{2q-1})} + \frac{\mathcal{B}^{(-)}_q}{0 - \mathrm{i}(\xi + r^{(2)}_{2q-1})}\right\} \\ &+\sum_{i=1}^{p}\left\{\frac{\mathcal{C}^{(+)}_i}{0 - \mathrm{i}(\xi - h_{2i})} + \frac{\mathcal{C}^{(-)}_i}{0 - \mathrm{i}(\xi + h_{2i})}\right\} + \frac{\mathcal{A}_0}{0 - \mathrm{i}\xi}\Bigg), \end{aligned} \tag{C.4}$$

$$\begin{aligned} u^F_{0,-} = -\frac{L_-}{\mu}\Bigg(&\sum_{w=1}^{z+1}\left\{\frac{\mathcal{A}^{(+)}_w}{0 + \mathrm{i}(\xi - r^{(1)}_{2w-1})} + \frac{\mathcal{A}^{(-)}_w}{0 + \mathrm{i}(\xi + r^{(1)}_{2w-1})}\right\} \\ &+\sum_{q=1}^{y+1}\left\{\frac{\mathcal{B}^{(+)}_q}{0 + \mathrm{i}(\xi - r^{(2)}_{2q-1})} + \frac{\mathcal{B}^{(-)}_q}{0 + \mathrm{i}(\xi + r^{(2)}_{2q-1})}\right\} \\ &+\sum_{i=1}^{p}\left\{\frac{\mathcal{C}^{(+)}_i}{0 + \mathrm{i}(\xi - h_{2i})} + \frac{\mathcal{C}^{(-)}_i}{0 + \mathrm{i}(\xi + h_{2i})}\right\} + \frac{\mathcal{A}_0}{0 + \mathrm{i}\xi}\Bigg). \end{aligned} \tag{C.5}$$

Then for the solution $u_0(\eta)$, the inverse Fourier transform should be applied in accordance with (3.12)–(3.14).

References

Ballarini, R., 1990. A rigid line inclusion at a bimaterial interface. Eng. Fract. Mech. 37 (1), 1–5.

Bigoni, D., Dal Corso, F., Gei, M., 2008. The stress concentration near a rigid line inclusion in a prestressed, elastic material. Part II. Implications on the shear band nucleation, growth and energy release rate. J. Mech. Phys. Solids 56 (2008), 839–857.

Carta, G., Jones, I.S., Brun, M., Movchan, N.V., Movchan, A.B., 2013. Crack propagation induced by thermal shocks in structured media. Int. J. Solids Struct. 50, 2725–2736.

Colquitt, D.J., Nieves, M.J., Jones, I.S., Movchan, N.V., Movchan, A.B., 2012. Trapping of a crack advancing through an elastic lattice. Int. J. Eng. Sci. 61, 129–141.

Colquitt, D.J., Nieves, M.J., Jones, I.S., Movchan, N.V., Movchan, A.B., 2013. Localisation for a line defect in an infinite square lattice. Proc. R. Soc. A 469, 20120579.

Craster, R.V., Kaplunov, J., Postnova, J., 2010. High-frequency asymptotics, homogenisation and localisation for lattices. Q. J. Mech. Appl. Math. 63 (4), 497–519.

Dal Corso, F., Bigoni, D., Gei, M., 2008. The stress concentration near a rigid line inclusion in a prestressed, elastic material. Part I. Full-field solution and asymptotics. J. Mech. Phys. Solids 56, 815–838.

Hills, N.L., 1965. Semi-infinite diffraction gratings. II. Inward resonance. Commun. Pure Appl. Math. 18, 389–395.

Hills, N.L., Karp, S.N., 1965. Semi-infinite diffraction gratings – I. Commun. Pure Appl. Math. 18, 203–233.

Hochstadt, H., 1989. Integral Equations. John Wiley & Sons, New York.

Koiter, W.T., 1964. Couple-stresses in the theory of elasticity, I and II. Proc. K. Ned. Akad. Wet. Ser. B 67, 17–44.

Mishuris, G.S., Movchan, A.B., Slepyan, L.I., 2009a. Localization and dynamic defects in lattice structures. In: Ruiz, P.D., Silberschmidt, V.V. (Eds.), Computational and Experimental Mechanics of Advanced Materials, CISM International Centre for Mechanical Sciences. Springer, pp. 51–82.

Mishuris, G.S., Movchan, A.B., Slepyan, L.I., 2009b. Localised knife waves in a structured interface. J. Mech. Phys. Solids 57, 1958–1979.

Mishuris, G., Piccolroaz, A., Radi, E., 2012. Steady-state propagation of a Mode III crack in couple stress elastic materials. Int. J. Eng. Sci. 61, 112–128.

Morini, L., Piccolroaz, A., Mishuris, G., Radi, E., 2013. On the fracture criteria for dynamic crack propagation in elastic materials with couple stresses, Int. J. Eng. Sci. 71, 45–61.

Movchan, A.B., Haq, S., Movchan, N.V., 2007. Localised defect modes and a macro-cell analysis for dynamic lattice structure with defects. In: Vibration Problems ICOVP 2005, Springer Proceedings in Physics, vol. 111, pp. 327–336.

Movchan, A.B., Brun, M., Movchan, N.V., 2012. Wave defect modes in structured media. In: Romeo, F., Ruzzene, M. (Eds.), Wave Propagation in Linear and Nonlinear Periodic Media, Analysis and Applications, International Centre for Mechanical Sciences, Courses and Lectures, vol. 540. Springer, Vienna, pp. 1–31.

Nieves, M.J., Movchan, A.B., Jones, I.S., Mishuris, G.S., 2013. Propagation of Slepyan's crack through a non-uniform elastic lattice. J. Mech. Phys. Solids 61, 1464–1488.

Noble, B., 1958. Methods Based on the Wiener–Hopf Technique for the Solution of Partial Differential Equations. International Series of Monographs on Pure and Applied Mathematics, vol. 7. Pergamon Press, New York.

Osharovich, G.G., Ayzenberg-Stepanenko, M.V., 2012. Wave localization in stratified square-cell lattices: the antiplane problem. J. Sound Vib. 331, 1378–1397.

Özturk, T., Poole, W.J., Embury, J.D., 1991. The deformation of Cu–W laminates. Mater. Sci. Eng. A 148, 175–178.

Slepyan, L.I., 2001a. Feeding and dissipative waves in fracture and phase transition. I. Some 1D structures and a square-cell lattice. J. Mech. Phys. Solids 49, 469–511.
Slepyan, L.I., 2001b. Feeding and dissipative waves in fracture and phase transition. II. Phase-transition waves. J. Mech. Phys. Solids 49, 513–550.
Slepyan, L.I., 2001c. Feeding and dissipative waves in fracture and phase transition. III. Triangular-cell lattice. J. Mech. Phys. Solids 49, 2839–2875.
Slepyan, L.I., 2002. Models and Phenomena in Fracture Mechanics. Springer, Berlin.
Slepyan, L.I., Ayzenberg-Stepanenko, M.V., 2004. Localized transition waves in bistable-bond lattices. J. Mech. Phys. Solids 52, 1447–1479.